JGR Solid Earth

RESEARCH ARTICLE
10.1029/2018JB016765

Slow Slip Event On the Southern San Andreas Fault Triggered by the 2017 M_w8.2 Chiapas (Mexico) Earthquake

Ekaterina Tymofyeyeva[1,2], Yuri Fialko[1], Junle Jiang[1,3], Xiaohua Xu[1], David Sandwell[1], Roger Bilham[4], Thomas K. Rockwell[5], Chelsea Blanton[5], Faith Burkett[5], Allen Gontz[5], and Shahram Moafipoor[6]

[1]Institute of Geophysics and Planetary Physics, Scripps Institution of Oceanography, University of California San Diego, La Jolla, CA, USA, [2]Now at Jet Propulsion Laboratory, California Institute of Technology, Pasadena, CA, USA, [3]Now at Department of Earth and Atmospheric Sciences, Cornell University, Ithaca, NY, USA, [4]CIRES and Geological Sciences, University of Colorado, Boulder, CO, USA, [5]Department of Geological Sciences, San Diego State University, San Diego, CA, USA, [6]Geodetics Inc., San Diego, CA, USA

Key Points:
- We present geodetic and geologic observations of slow slip on the southern SAF triggered by the 2017 Chiapas (Mexico) earthquake
- The slow slip event produced surface offsets on the order of 5–10 mm, with significant variations along strike
- We interpret the observed complexity in shallow fault slip in the context of rate-and-state friction models

Supporting Information:
- Supporting Information S1

Correspondence to:
E. Tymofyeyeva,
katia.tymofyeyeva@gmail.com

Citation:
Tymofyeyeva, E., Fialko, Y., Jiang, J., Xu, X., Sandwell, D., Bilham, R., et al. (2019). Slow slip event on the southern San Andreas fault triggered by the 2017 M_w8.2 Chiapas (Mexico) earthquake. *Journal of Geophysical Research: Solid Earth*, *124*. https://doi.org/10.1029/2018JB016765

Received 23 SEP 2018
Accepted 29 JUL 2019
Accepted article online 4 AUG 2019

Abstract Observations of shallow fault creep reveal increasingly complex time-dependent slip histories that include quasi-steady creep and triggered as well as spontaneous accelerated slip events. Here we report a recent slow slip event on the southern San Andreas fault triggered by the 2017 M_w8.2 Chiapas (Mexico) earthquake that occurred 3,000 km away. Geodetic and geologic observations indicate that surface slip on the order of 10 mm occurred on a 40-km-long section of the southern San Andreas fault between the Mecca Hills and Bombay Beach, starting minutes after the Chiapas earthquake and continuing for more than a year. Both the magnitude and the depth extent of creep vary along strike. We derive a high-resolution map of surface displacements by combining Sentinel-1 Interferometric Synthetic Aperture Radar acquisitions from different lines of sight. Interferometric Synthetic Aperture Radar-derived displacements are in good agreement with the creepmeter data and field mapping of surface offsets. Inversions of surface displacement data using dislocation models indicate that the highest amplitudes of surface slip are associated with shallow (<1 km) transient slip. We performed 2-D simulations of shallow creep on a strike-slip fault obeying rate-and-state friction to constrain frictional properties of the top few kilometers of the upper crust that can produce the observed behavior.

1. Introduction

A number of active continental strike-slip faults are associated with geodetically detectable shallow creep, while other faults (or other sections of the same fault) appear to be locked all the way to the surface over the interseismic period (e.g., Cakir et al., 2005; Harris, 2017; Lindsey, Sahakian, et al. 2014; Lindsey & Fialko, 2016; Savage & Lisowski, 1993; Simpson et al., 2001). Traditional interpretations of shallow creep in terms of the conditionally stable or velocity-strengthening (VS) friction in the uppermost crust predict that shallow creep should occur at a quasi-constant rate throughout much of the earthquake cycle (e.g., Kaneko et al., 2013; Li & Rice, 1987; Lindsey & Fialko, 2016; Marone & Scholz, 1988). However, geodetic observations indicate that faults that exhibit shallow creep also often host episodic accelerated creep events (e.g., Bilham et al., 2016; Goulty & Gilman, 1978; Jolivet et al., 2015; Linde et al., 1996; Murray & Segall, 2005; Wei et al., 2009; Shirzaei & Bürgmann, 2013), similar to the extensively studied episodic slow slip at the bottom of seismogenic megathrusts in subduction zones (Obara et al., 2004; Rogers & Dragert, 2003; Schwartz & Rokosky, 2007). Transient creep events have been also detected in shallow sections of subduction megathrusts (e.g., Araki et al., 2017; LaBonte et al., 2009; Wallace et al., 2016). Slow slip events can occur spontaneously or be triggered by static or dynamic stress changes due to nearby or distant earthquakes (Allen et al., 1972; Rymer et al., 2010; Simpson et al., 2001; Wei et al., 2010; Wei, Yajing, et al., 2015).

One of the well-known examples of an active continental fault exhibiting shallow creep is the southern section of the San Andreas Fault in California (Figure 1; Allen et al., 1972; Bilham & Williams, 1985; Fialko, 2006; Goulty & Gilman, 1978; Lindsey, Fialko, et al., 2014; Lyons & Sandwell, 2003; Manzo et al., 2012; Wei et al., 2010). Sieh and Williams (1990) estimated an average creep rate on the southern San Andreas

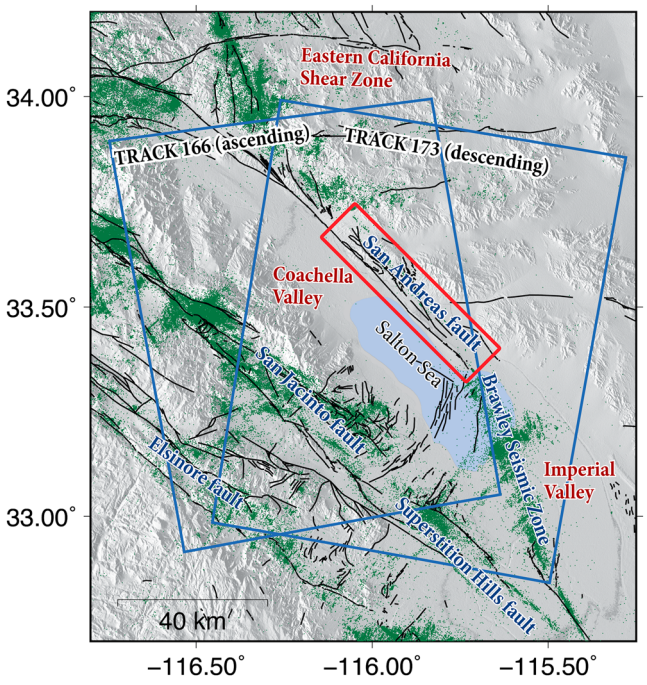

Figure 1. Map of the study area. Green dots denote seismicity (Hauksson et al., 2012), and black wavy lines denote active faults (Jennings & Bryant, 2010). The red rectangle outlines a section of the southern San Andreas fault involved in a recent shallow slow slip event. Blue rectangles denote subswaths of Sentinel-1 acquisitions used in this study.

fault (SSAF) of 2–4 mm/year, based on creepmeter measurements, and offsets of man-made structures and well-dated geologic features corresponding to time intervals of several years to a few hundred years. This is in good agreement with the average surface creep velocities obtained from the Envisat Interferometric Synthetic Aperture Radar (InSAR) observations spanning 2004–2010 (Lindsey, Fialko, et al., 2014), suggesting that the average rate of shallow creep on the SSAF may be essentially constant over time scales on the order of 10 years or greater. The average value of the surface creep rate of a few millimeters per year is consistent with the estimated slip rate on the SSAF of ~18 mm/year (Behr et al., 2010; van der Woerd et al., 2006; Lindsey & Fialko, 2013), provided the depth extent of shallow creep is on the order of a few kilometers (Kaneko et al., 2013; Li & Rice, 1987; Lindsey & Fialko, 2016; Savage & Lisowski, 1993; Tymofyeyeva & Fialko, 2018; Wei et al., 2009).

Instrumental measurements of surface creep on the SSAF, however, indicate that the creep is not steady and is punctuated by episodes of accelerated slip that can last days to months (Allen et al., 1972; Schulz et al., 1983; Sieh & Williams, 1990), similar to observations from the nearby Superstition Hills fault (Bilham & Behr, 1992; Wei et al., 2009). Some of the observed slip events on the SSAF were triggered by shaking from regional earthquakes (Allen et al., 1972; Lyons & Sandwell, 2003; Rymer, 2000; Rymer et al., 2002, 2010; Wei et al., 2010), while others appear to have occurred spontaneously.

The physical mechanisms and conditions giving rise to shallow transient slip are not well understood. Wei et al. (2013) and Wei, Yajing, et al. (2015) proposed that the observed variability in the styles of surface creep (quasi-steady, spontaneous, and triggered slip) on the Superstition Hills fault can be explained by the nucleation of slip in a velocity-weakening (VW) layer embedded in the top several kilometers of the VS uppermost crust. Such an interpretation implies rather special lithological conditions and may not be applicable to a variety of locations where episodic shallow slip has been detected. In this study, we present geodetic and geologic observations of a recent shallow creep event on the SSAF triggered by the 2017 M8.2 Chiapas (Mexico) earthquake, which occurred on 7 September at 23:49 local time (8 September, 04:49 UTC; Heidarzadeh et al., 2018; Jimenez, 2018). We combine measurements from InSAR, creepmeters, and geologic mapping, to document the triggered fault creep at high spatial and temporal resolution. We then use numerical models to explore friction properties of the shallow crust that can give rise to the observed behavior.

2. Geodetic and Geologic Observations of a Recent Creep Event on the SSAF

2.1. Creepmeter Measurements

Seven creepmeters installed along active faults in Southern California monitor surface slip history at high sampling rate. Creepmeters deployed on the SSAF are listed in Table 1. The creepmeters (extensometers)

Table 1
Creepmeter Location, Triggered Dextral Slip, and Distance From North Shore

Site	Location	Lat ° N	Lon ° W	ϕ	Ref	L m	Azi°	km	8 Sep 29 Nov	30 Nov 29 Jan
coNS	North Shore	33.531	115.939	45°	Fe	10	103	0	0.39±.02	1.53±.02
coFE	Ferrum	33.457	115.854	30°	C	9	103	11.2	2.86±.02	0.88±.02
sc72	Salt Creek	33.448	115.844	72°	C	11.8	61	12.6		
sc30	Salt Creek	33.448	115.844	30°	C	12.8	103	12.6	2.79±.02	0.55±.02
coDU	Durmid Hill	33.412	115.795	30°	C	14	103	18.2	0.85±.02	1.21±.02
sh30	Shoreline F.	33.371	115.7801	30°	C	13	109	23.0	0.17±.02	0.03±.02
sh90	Shoreline F.	33.371	115.7801	90°	C	11	136	23.0		

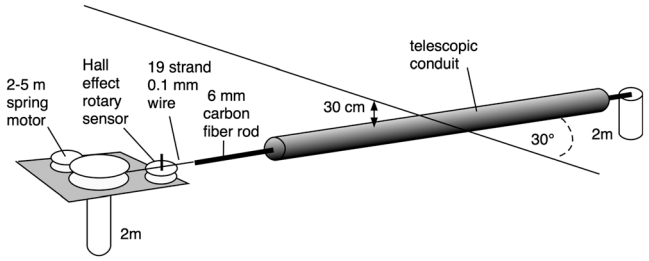

Figure 2. Schematic view of buried creepmeter installed obliquely across a fault. A thin nylon-coated multistrand stainless wire attached to the free end of the rod is held in tension by a 0.5-N constant-tension spring motor. The wire is wrapped once around the shaft of a 360° rotary Hall-effect sensor such that one complete revolution corresponds to a 10-mm translation of the carbon fiber rod through the fault zone. The lengths of the seven creepmeters (L = 9–14 m), their installation azimuths, and their obliquities to the local strike of the fault (ϕ = 30–90°) are listed in Table 1.

are installed within the surface shear zone and provide a continuous time history of slip with sampling intervals between 2 s and 30 min. Each extensometer consists of an inextensible reference rod (a continuous 4-mm diameter carbon fiber) enclosed within a telescopic polyvinyl chloride tube buried at 30° to the strike of the fault, crossing the fault at a depth 0.3–1.5 m (Figure 2). One end of the rod is anchored rigidly to the subsurface, and the motion of the free end is measured relative to a similar anchor on the far side of the fault using a displacement sensor. The sensors are rotary Hall-effect sensors with 6-μm resolution and 2.4-m range (Bilham et al., 2004). The creepmeters described here sample fault zone widths of 4.5–7 m, approximately half their operating length (Table 1). Two of the creepmeters are refurbished Caltech instruments (Louie et al., 1985; McGill et al., 1989). In 2015 the Salt Creek creepmeter steel reference wire was replaced with a carbon fiber rod and a second creepmeter installed at 30° to the fault. The North Shore creepmeter retains its original stainless steel length standard.

In the 18 months prior to the Chiapas earthquake (Figure 3), slow steady slip of less than 2 mm/year was being recorded on all the creep sensors operating on the SSAF, with minor rate changes mostly due to diurnal thermoelastic effects. Creep rates at Ferrum were effectively zero following a 0.5-mm creep event in December 2014. Within 20 min of the earthquake, which occurred at 04:49 UTC, dextral slip rates at three of the sites had accelerated to 10–36 μm/s, with slip magnitude increasing to a few millimeters in the next 2 days (Table 1), equivalent to a whole year of creep at pre-Chiapas rates.

The time for surface waves from Chiapas to arrive at Durmid Hill was approximately 16.5 min, and these waves would have traversed the entire 23-km-long creep array in ~6.5 s. The low sampling rates (5–30 min) do not permit us to determine the precise time that slip started at each site, but slip at Ferrum was 30 μm 11 min after the mainshock and 300 μm after 41 min. At Salt Creek no slip was registered until 22 min after the mainshock. Slip at Durmid Hill did not occur until 64 min after the mainshock, and no slip occurred at North Shore, 12.6 km to the north, until a day later. Normally, a 24-hr delay between the passage of surface waves and fault slip would not be associated with remote triggering; however, the North Shore location is unusual in that hitherto no event-like slip has previously been recorded there. Although no slip occurred on 8 September on the newly identified Shoreline fault near Bombay Beach (Jänecke et al., 2018), its subsequent slip of 0.25 mm may represent the first time that a tectonic response has been recorded on the fault.

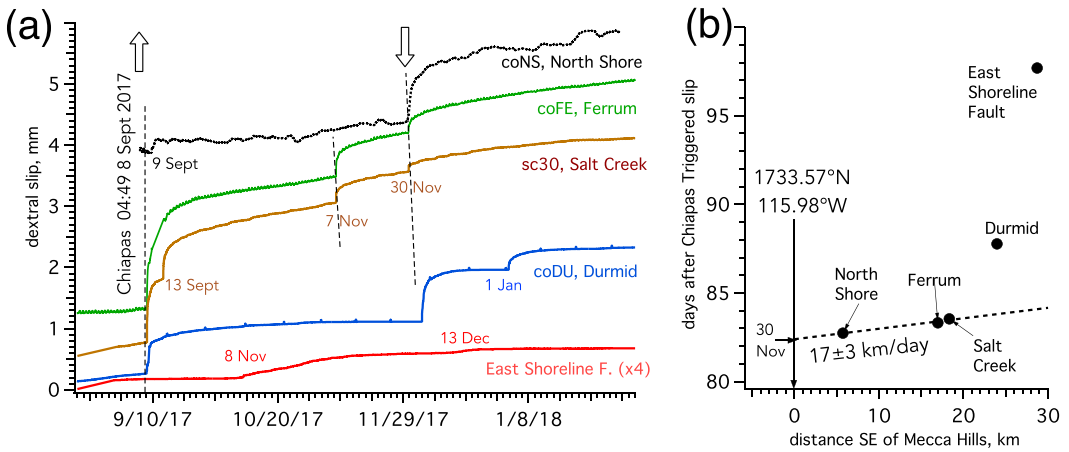

Figure 3. (a) The Chiapas earthquake initiated a slip episode within 13 min of the Chiapas earthquake with minor slip at North Shore 27.35 hr later consistent with northward propagation. Dates of aseismic subevents are indicated. A southward propagating slip event on 30 November that may have nucleated in the Mecca Hills was recorded by all five extensometers, albeit weakly by the East Shoreline extensometer. The 7 November slip event also propagated southward but was recorded only at Ferrum and Salt Creek. (b) The southward propagation velocity between the first three sites was 17 ± 3 km/day.

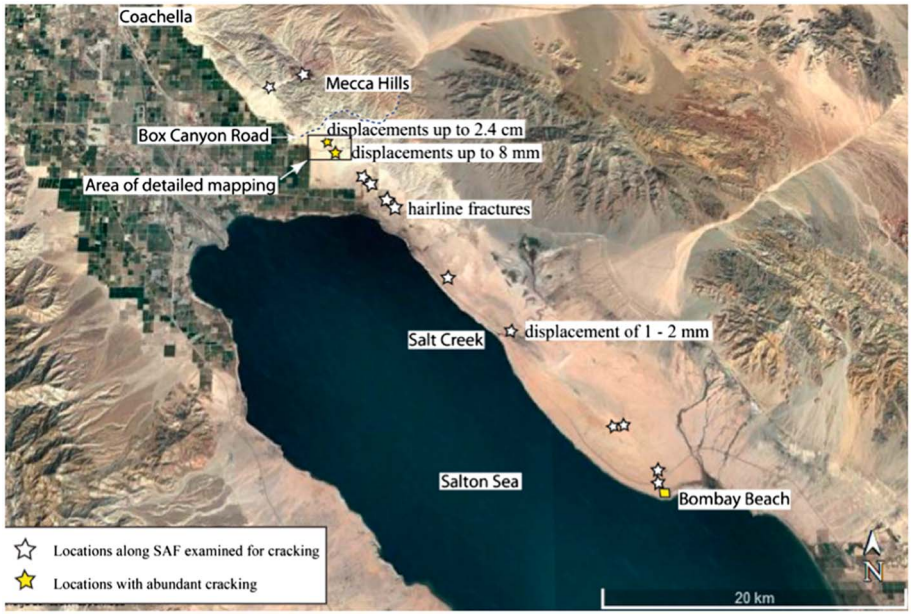

Figure 4. Fault locations where triggered slip was investigated. Minor cracking was noted at Salt Creek, and fracturing, interpreted as possible surface cracking, was found near North Shore. Significant rupture with measurable offsets were found in the "area of detailed mapping." SAF = San Andreas fault.

We conclude that surface slip on the San Andreas fault following the Chiapas earthquake occurred at (or close to) the time of passage of surface waves from the main shock.

2.2. Field Mapping of Surface Offsets

Two days were spent in the field mapping surface evidence of the creep event and measuring surface displacements. We conducted the field survey on 23 February and 1 March 2018, focusing on the fault from the Mecca Hills southeast to the town of Bombay Beach (Figure 4). We found fresh en echelon cracking with small right-lateral displacements (3–24 mm) for 2.4 km along the San Andreas fault from 0.4 km SE of Box Canyon Road southeastward to 0.75 km SE of the Coachella Canal (Figure S1 in the supporting information), and minor cracking (1–2 mm of possible right-lateral offset) in a small wash about 40 m NW of the Salt Creek creep meter (Figure 4).

All other sites visited showed no evidence of recent displacement except near the town of North Shore where we observed some hairline fractures that could possibly be attributed to the fault. An interesting side note is that surface cracks bisected a fire ring inferred to be offset by the SSAF (Shifflett et al., 2002), confirming that the irregular shape of the fire ring is likely due to fault slip, most or all of which could be attributed to shallow creep.

We surveyed the location of the crack in the field with hand-held GPS (Garmin MAP 64ST) and collected far more crack location points than offset measurements (Figure S1). The displacements were measured with a steel tape along the strike direction of the San Andreas fault. For most measurements, we located very small, centimeter-scale dilational steps and bends and measured the width of opening across these microbasins (Figure 5). We cannot preclude small amounts of erosion of the microbasin walls, although we primarily measured features that displayed excellent matches of the opposing wall morphology. Nevertheless, we estimate uncertainties of a few millimeters for all measurements. The along-fault slip distribution measured in the Box Canyon area is shown in Figure S2.

2.3. InSAR Measurements

We analyzed data from the Sentinel-1 mission of the European Space Agency, collected between the years 2015–2019. We used Subswaths 1 and 2, respectively, from Sentinel-1 ascending and descending tracks 166 and 173 that cover the area of interest (Figure 1). The data were processed at full resolution (without multilooking) using GMTSAR (Xu et al., 2016). All radar images were aligned to a single master using the bivariate enhanced spectral diversity method (Wang et al., 2017). We then formed interferograms between each successive pair of acquisitions, resulting in a set of 84 sequential interferograms from ascending track

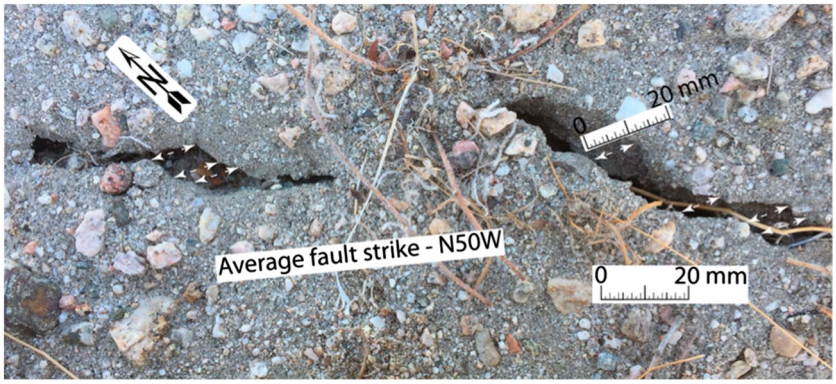

Figure 5. Example of en echelon surface rupture associated with creep event showing the small dilational steps used to measure displacement. Displacement in this example is estimated at 11 mm.

166 and 82 interferograms from descending track 173. Baseline plots for the respective tracks are shown in Figure S3. Topographic phase was removed using a TanDEM-X digital elevation model with 12-m postings (Moreira et al., 2004). Interferograms were filtered using a 100-m Gaussian filter and an adaptive Goldstein filter (Goldstein & Werner, 1998) and unwrapped using the SNAPHU algorithm (Chen & Zebker, 2000).

To investigate the spatiotemporal evolution of the shallow slip event on the SSAF, we calculated a time history of range changes by incrementally adding phase from sequential interferograms. We found that summation of a large number of interferograms introduces high-frequency spatial noise that is not present in "direct" interferograms formed using any two given SAR acquisitions. This problem (also noted by Lau et al., 2018) arises from errors introduced during filtering of the radar phase prior to phase unwrapping. This can be demonstrated using a circuit closure test, that is, by computing the difference between the sum of the radar phase from N sequential interferograms, and a direct interferogram spanning the entire time period between the first and last acquisitions. The mean of the difference as a function of N is shown in Figure S4 (red dots). The circuit nonclosure errors accumulate progressively as more interferograms are added. One can demonstrate that the nonclosure errors result from filtering, because the same test using nonfiltered wrapped interferograms yields a much better circuit closure (Figure S4, black dots). Figure S5 shows the spatiotemporal variations in the circuit closure errors in the area of interest.

To improve the accuracy of the InSAR time series, it is therefore desirable to avoid filtering of the radar phase. Phase filtering is a standard procedure in processing of InSAR data; in particular, it considerably facilitates phase unwrapping. In case of a reasonably high coherence of radar images, one can take the difference between filtered and unfiltered wrapped phase (modulo 2π) and subtract it from the filtered unwrapped phase. The result is the unfiltered unwrapped phase. The latter satisfies the circuit closure test if the errors introduced by filtering are smaller than $\pm\pi$ radians. Pixels that do not satisfy this condition are subject to phase ambiguity errors equivalent to phase unwrapping errors. In principle, such ambiguities can be identified and corrected by enforcing circuit closure using redundant interferograms for the entire data set. Here we simply used circuit closure to identify and mask out pixels affected by the phase ambiguity errors after the "unfiltering" procedure. Unless otherwise noted, all results presented below were obtained using the unfiltered interferograms.

We estimated contributions to the radar phase due to propagation of the radar signal through the atmosphere using the common scene stacking method (Tymofyeyeva & Fialko, 2015). To minimize temporal smoothing around the onset of triggered slip, we used averaging stencils of variable aperture. The latter is increased from two nearest data takes around 8 September 2017, to eight nearest data takes toward the beginning and the end of the time series. After estimating atmospheric phase screens for all acquisitions, the former were removed from the interferograms.

We generated time series of LOS displacements by adding phase from sequential interferograms corrected for the atmospheric delays. To compute LOS displacements over a given period of time, we fitted a smoothing spline to the time series and took the difference between the respective points of the spline fit. Because the common scene stacking method does not suppress atmospheric artifacts that are nonrandom in time (e.g., seasonal variations in the stratified water vapor), we corrected the LOS displacement data by subtracting the

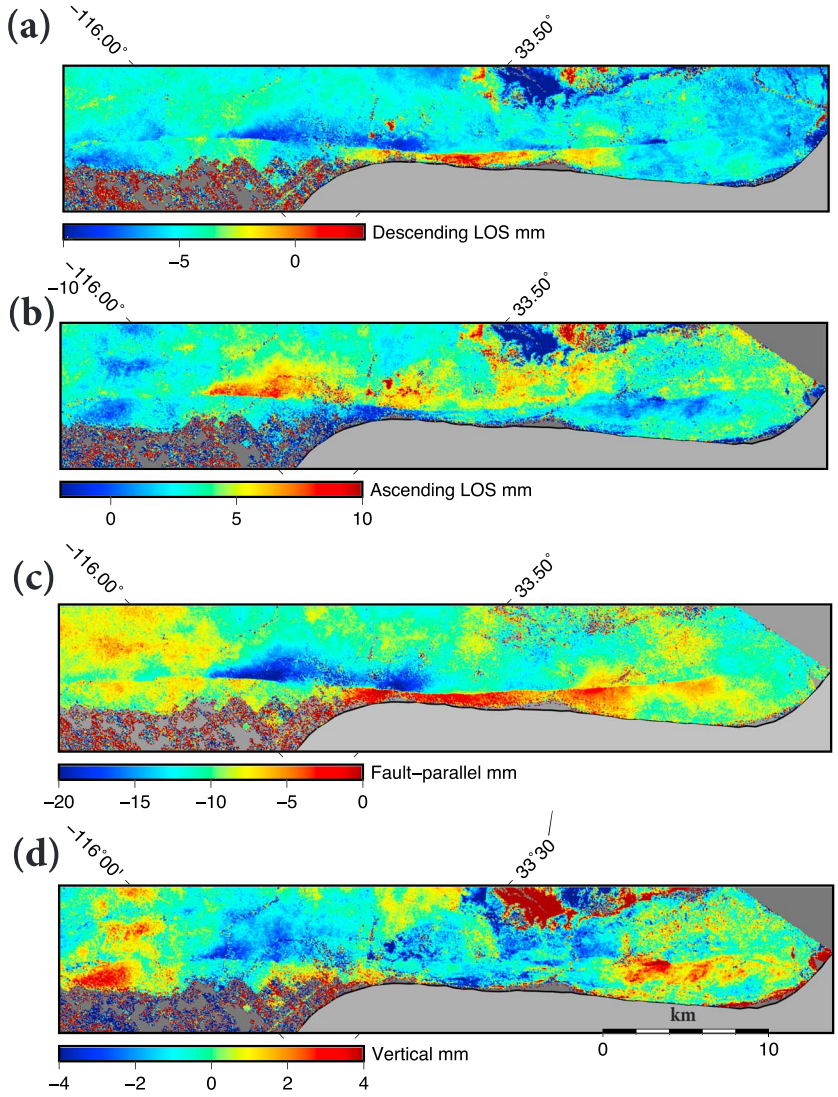

Figure 6. Line-of-sight (LOS) displacements from (a) ascending (166) and (b) descending (173) Sentinel-1 tracks and the inferred (c) fault-parallel and (d) vertical components of surface displacements over a time period of 6 months following the 2017 Chiapas earthquake.

best linear fit between the LOS displacements and topography. Finally, to mitigate residual long-wavelength artifacts in the LOS displacements and to bring data from different lines of sight into the same reference frame, we constrained the LOS displacements to agree with the interpolated displacements obtained from the GPS data (Figure S6) at wavelengths greater than 20 km using the remove-restore method (Tong et al., 2013). Figures 6a and 6b show the LOS displacements from the ascending and descending tracks over the time period of 6 months following the 2017 Chiapas earthquake.

InSAR data from the ascending and descending tracks can be used to derive the fault-parallel and vertical components of the displacement field under the assumption that the fault-perpendicular component of motion is negligible (Fialko et al., 2001; Lindsey, Fialko, et al., 2014):

$$\begin{bmatrix} e_a \sin(\alpha) + n_a \cos(\alpha) & u_a \\ e_d \sin(\alpha) + n_d \cos(\alpha) & u_d \end{bmatrix} \begin{bmatrix} D_H \\ D_V \end{bmatrix} = \begin{bmatrix} D_a \\ D_d \end{bmatrix}, \quad (1)$$

where D_H and D_V are horizontal and vertical surface displacement components; e, n, and u are east, north, and up components of the unit look vectors for the ascending and descending satellite tracks (taking into account variations in the radar incidence angle); α is the local fault strike (Figure S7); and D_a and D_d are InSAR LOS displacements from the ascending and descending tracks, respectively. Figures 6c and 6d show

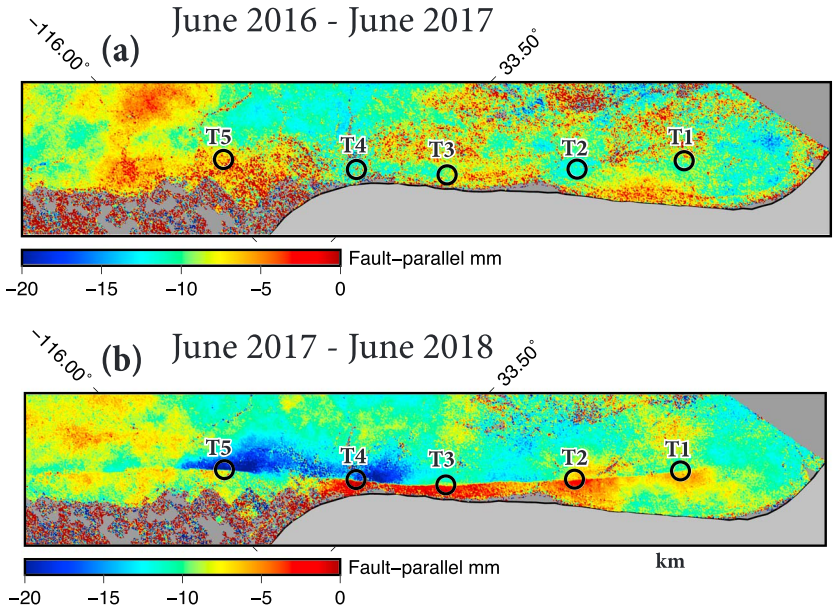

Figure 7. Fault-parallel displacements (a) 1 year before the September 2017 triggering event (June 2016 to June 2017) and (b) the following year (June 2017 to June 2018).

the fault-parallel and vertical displacements over the time period of 6 months following the 2017 Chiapas earthquake.

A comparison of fault-parallel displacements that occurred over time periods of 1 year before (June 2016 to June 2017; Figure 7a) and 1 year after (June 2017 to June 2018; Figure 7b) the Chiapas earthquake indicates that there was little surface creep along the SSAF in years before the Chiapas earthquake (except for the southernmost section near Durmid Hill), in agreement with the creepmeter measurements. It follows that the displacement discontinuity seen in Figure 7 is predominantly due to shallow slip that occurred following the Chiapas earthquake.

To investigate the time dependence of shallow creep on the SSAF, we differenced the displacements between points located on either side of the fault, at a distance of 450 m away from the fault trace, to capture possible contributions from shear distributed in a finite fault zone (Fialko et al., 2002; Lindsey, Sahakian, et al., 2014; Lindsey, Fialko, et al., 2014). Figure S8 shows examples of time series of LOS displacements at two locations along the SSAF (see Figure 7), before and after applying the atmospheric corrections. The LOS displacements were computed by averaging radar phase over a 80 by 80 m window centered on the respective query points. Uncertainties (denoted by vertical error bars in Figure S5) were obtained by computing a synthetic set of interferograms using the estimated atmospheric phase screens, and applying the same procedure as employed for calculating the LOS displacement time series. Because no deformation signal is present in the synthetic interferograms, the recovered "displacements" are indicative of the measurement uncertainty.

We combined time series of the LOS displacements to evaluate the time history of differential fault-parallel motion using equation (1). Because acquisitions for the ascending and descending tracks were not coincidental in time, the LOS displacement time series for each track were resampled at a common interval of 24 days using spline fitting. Figure 8 shows the resulting time series at several points along the SSAF.

The time series shown in Figures 8 and S8 clearly reveal an onset of accelerated slip around the time of the Chiapas earthquake. At some locations the onset of slip appears to predate the earthquake (e.g., at Site T4, Figure 8a). Because the atmospheric corrections are expected to result in some smoothing of rapid temporal variations in surface velocities, it is uncertain whether the inferred "precursory" variations in the fault creep rate are processing artifacts or an indication that the earthquake triggering has accelerated a slow slip event that was already underway.

To quantify the extent and variations of triggered slip along the strike of the SSAF, we computed the difference in fault-parallel displacements derived from InSAR data on opposite sides of the fault at multiple

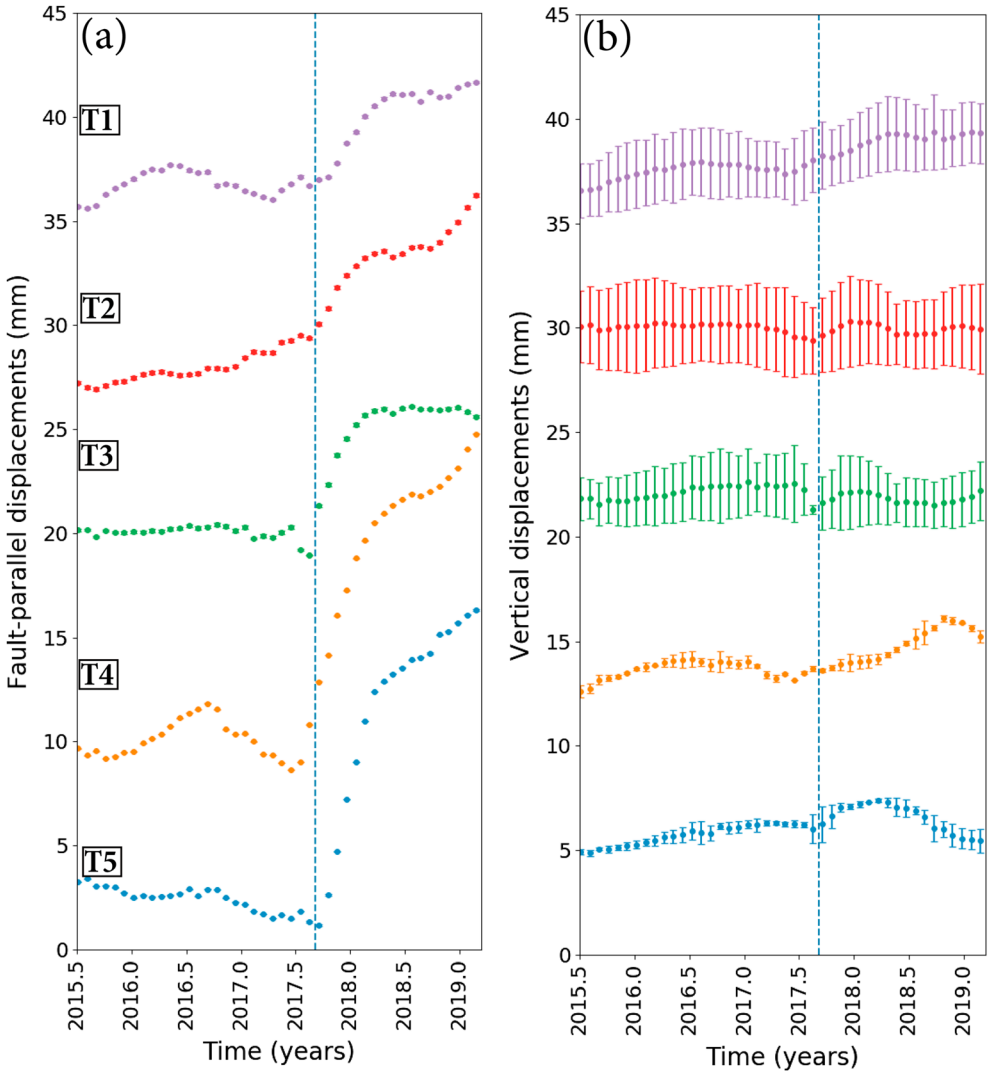

Figure 8. Time series of fault-parallel and vertical displacements, along with uncertainties, derived using unfiltered unwrapped interferograms. The point locations are shown in Figure 7. The dashed vertical line denotes the time of the 2017 Chiapas earthquake.

locations along the fault trace (Figure 9b, black circles). In order to provide a meaningful comparison between the offsets from InSAR measurements to the relatively small-aperture creepmeter and geologic measurements, we sampled the displacements 100 m away from the fault, within an averaging window of 50 m around each query point. To quantify errors associated with each measurement, we formed synthetic interferograms by differencing atmospheric phase screens corresponding to the acquisition dates of interferograms used in the analysis, propagated the synthetic interferograms through the two-component displacement decomposition described above, and queried the respective points along the fault trace. The results are shown in Figure 9a, along with a comparison to the measurements collected during the field survey (section 2.2; also, see Figure S9) and by the creepmeters (denoted by purple squares in Figure 9). The locations of all the query points are marked in Figure 9b.

Figure S10 shows profiles of displacements across the fault trace at several sites corresponding to the creepmeter locations (section 2.1). The respective sites are outlined with white rectangles in Figure S10e. We collapsed the InSAR-derived displacements inside each of the white rectangles onto a one-dimensional profile and plotted them with respect to the distance across the fault, from southwest to the northeast. The profiles are shown in the top four panels of Figure S10. Offsets on the order of several millimeters are clearly seen in every profile.

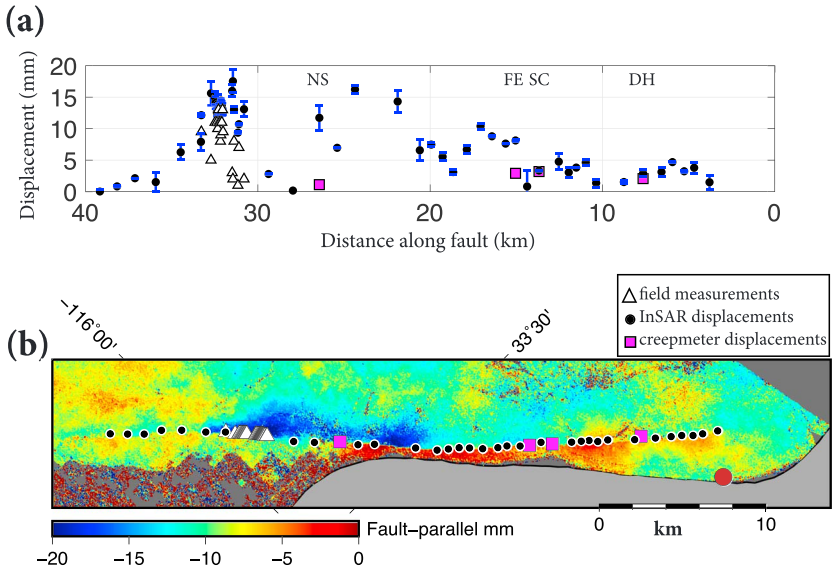

Figure 9. Distribution of triggered slip along the fault. (a) Displacement profile. (b) Displacement map. White triangles represent measurements made during the field survey, purple squares represent creepmeter data, and black circles represent Interferometric Synthetic Aperture Radar data. The abbreviations "NS," "FE," "SC," and "DH" in the top panel represent the names of the creepmeters corresponding to the purple squares, and stand for "North Shore," "Ferrum," "Salt Creek," and "Durmid Hill," respectively. The location of the Shoreline creepmeter is plotted as a brown circle. Interferometric Synthetic Aperture Radar data were sampled 100 m away from the fault trace.

3. Modeling of Triggered Creep

3.1. Estimating the Depth of Triggered Creep

We estimated the depth extent of triggered slip and the shallow fault attitude at several locations along the SSAF using a simple kinematic model consisting of two screw dislocations in a semi-infinite, homogeneous, elastic half-space: one dislocation representing shallow creep and another representing the long-wavelength interseismic deformation. In this case, surface displacements in the fault-perpendicular direction can be described as follows:

$$D(x) = \frac{V_{\mathrm{pl}} t}{\pi} \tan^{-1}\left(\frac{x-\xi_l}{d_l}\right) + \frac{s_s}{2}\mathrm{sgn}(x) - \frac{s_s}{\pi}\tan^{-1}\left(\frac{x-\xi_s}{d_s}\right), \tag{2}$$

where $D(x)$ represents the fault-parallel surface displacements at a distance x away from the fault, V_{pl} is the long-term fault slip rate, t is the time period of observations, d_l is the depth of locking at the bottom of the seismogenic layer, and d_s and s_s are the depth extent and amplitude of shallow creep, respectively. Parameters ξ_l and ξ_s represent offsets of the edges of the respective dislocations with respect to the fault trace in case of a nonvertical fault geometry:

$$\xi_l = \frac{d_l}{\tan(\theta_l)},\ \xi_s = \frac{d_s}{\tan(\theta_s)}, \tag{3}$$

where θ_s and θ_l are the average dip angles of the fault in the shallow creeping layer and the entire upper crust, respectively. Parameters for the deep dislocation were constrained based on the best fitting models of Lindsey and Fialko (2013): $d_l = 12$ km, $V_{\mathrm{pl}} = 18$ mm/year multiplied by the time span of observations, and fault dip of 75° to the northeast. We solved for the slip s_s, depth extent d_s, and offset ξ_s (i.e., dip) of the shallow dislocation by performing a series of inversions using a Bayesian Markov Chain algorithm known as "slice sampling" (Neal, 2003). We chose the mean model out of 10^6 model runs (10^3 walks with 10^3 steps) at each location. The profiles used fault-parallel displacements derived from the unfiltered unwrapped radar phase (Figure 7b). Figure 10 shows the data, the best fit models, and the model uncertainties for several locations shown in Figure 7. The misfits on the order of a few millimeters are likely dominated by the residual atmospheric noise and phase decorrelation (in particular, on the western side of the fault).

3.2. Dynamic Stress Perturbations From Seismic Waves

To better understand the initiation conditions of the slow slip event, we used seismic observations to estimate dynamic stress perturbations on the SSAF due to passing seismic waves from the Chiapas earthquake

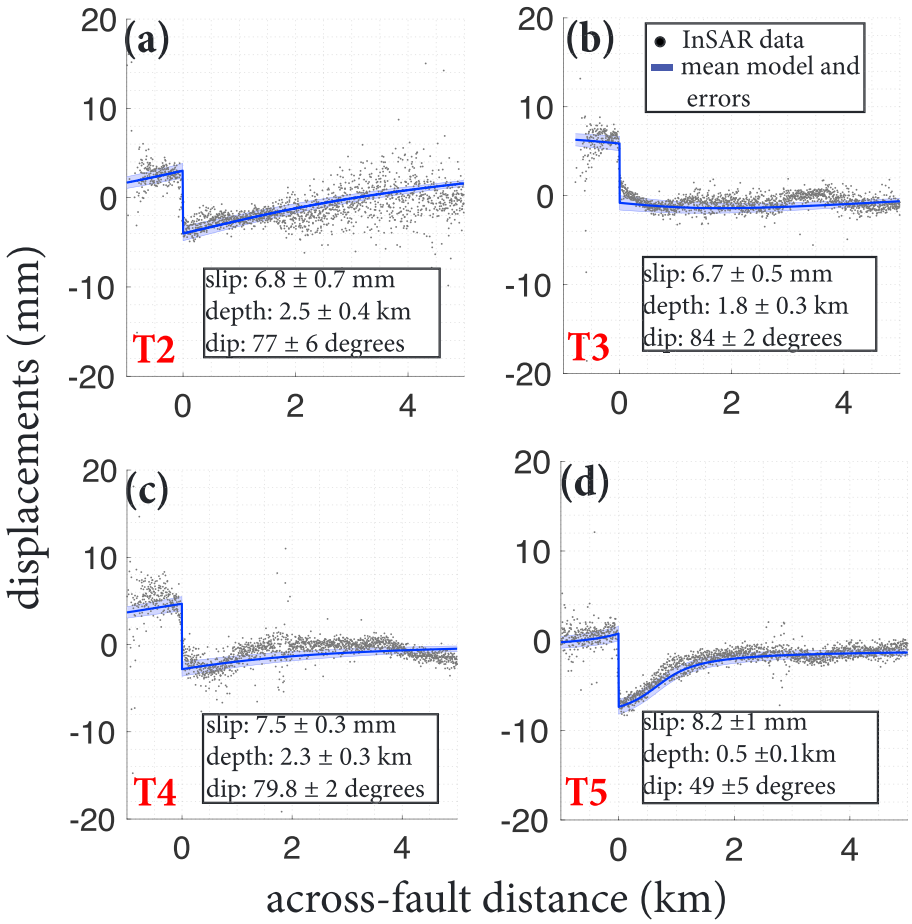

Figure 10. Results of inversions of surface displacements for the amplitude, depth, and dip of shallow creep. Panels (a)–(d) show profiles of fault-parallel displacements at several locations along the fault trace (see white circles in Figure 7b). Black dots denote Envisat Interferometric Synthetic Aperture Radar (InSAR) data, and blue lines denote the best fitting models. Shaded blue areas denote the model uncertainties. The respective model parameters are presented below each model.

(Figure 11). We consider five strong-motion stations closest to the San Andreas fault (Figure 11a). Because the velocity seismograms from these stations are highly similar (Figure S11), we aligned the waveforms to account for the difference in surface wave arrival times and took an average. The averaged velocity components are shown in Figures 11c–11e. As one can see in Figures 11c–11e, the amplitudes of body waves are insignificant compared to surface waves. In particular, the Love waves, as clearly shown in the transverse component, result in ground motion of up to 5 mm/s, almost twice as large as the motion associated with the Rayleigh waves seen in the radial and vertical components. The dominant periods of these seismograms are ~20–25 s, and the overall duration of ground shaking is ~300 s.

Assuming a plane-wave form for the surface waves, we can convert velocity seismograms, $V(t)$, to dynamic strains as follows: $\epsilon_{xx}=V_x/V_g$ and $\epsilon_{xy}=V_y/V_g$ (e.g., Gomberg & Bodin, 1994; Wei, Liu, et al. 2015), where ϵ_{xx} and ϵ_{xy} are the normal and shear components of dynamic strains along the fault, respectively, and V_g is the group velocity. We estimate the maximum dynamic strains to be $\sim 10^{-6}$ given an estimated V_g of 3.3 km/s. The waveform similarity supports the plane-wave approximation and indicates near-uniform stressing conditions on the SSAF. The dynamic strains can be used to compute the dynamic Coulomb stress changes on the fault: $\Delta\tau_c = \mu(\epsilon_{xy} - f_0\epsilon_{xx})$, where μ is the shear modulus and f_0 is the coefficient of friction. For $f_0 = 0.6$ and $\mu = 22$ GPa, we estimate dynamic stress perturbations to be ~30 kPa (Figure 11h). Since the back azimuth angle for the earthquake is close to the strike angle of the SSAF, the normal stress perturbations are produced predominantly by the Love waves, and the shear stress perturbations are produced predominantly by the Rayleigh waves. The two types of surface waves thus contribute comparably to the dynamic Coulomb stress changes on the fault and are both plausible sources for triggering slow slip on the SSAF.

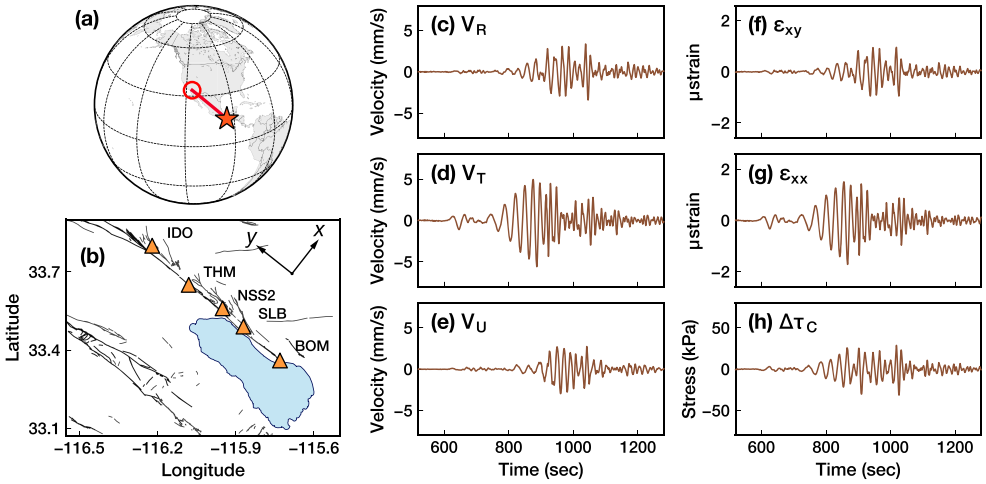

Figure 11. Dynamic stress perturbations from passing seismic waves. (a) A 3-D global view of the 2017 Chiapas earthquake location (star) and our study area (circle), with the connecting great-circle path in red. (b) The regional view of strong-motion stations (triangles) near the San Andreas fault. Surface traces of holocene and quaternary faults are marked in black, and the Salton Sea is drawn in blue. The *x*-*y* coordinate system is oriented along the fault-parallel and fault-perpendicular directions. (c–e) The radial, transverse, and vertical components of the averaged velocity seismograms (integrated from accelerograms). Waveforms are shifted to account for the difference in surface wave arrival times before averaging. (f–g) The normal and shear components of estimated dynamic strains, ϵ_{xx} and ϵ_{xy}, along the fault. (h) The estimated dynamic Coulomb stress change $\Delta\tau_c$.

3.3. Time-Dependent Creep on a Fault Obeying Rate-and-State Friction

Motivated by observations of unsteady shallow creep on the SSAF, we consider a fault model with a layered structure and a monotonic transition in the rate-and-state fault frictional properties above the seismogenic zone (Figure 12). In such a model, the shallow VS (stable) and mildly VW (conditionally stable) regions produce steady and unsteady fault creep, respectively, and interact with each other through elastic stress transfer. Given the average rate of shallow creep of ~3 mm/year, the long-term fault slip rate of ~18 mm/year, and a fault locking depth of ~12 km (Lindsey & Fialko, 2013), we estimate the depth of transition from the shallow creep to the locked seismogenic zone of ~2.5 km based on a stress-driven crack model (e.g., Savage & Lisowski, 1993), largely consistent with our estimates of the depth extent of creep using kinematic models (section 3.1).

In our stress-driven models, we consider a 1-D planar strike-slip fault embedded into a 2-D uniform linear elastic half-space. The fault plane extends to the free surface at the top and is prescribed with a fixed plate-loading rate, $V_{pl} = 20$ mm/year, below the seismogenic zone (depth $d_l = 11.5$ km). A fixed, much lower slip rate is assumed within the seismogenic zone in the depth range between d_s and d_l. On the shallow (depth smaller than $d_s = 2.7$) part of the fault, we adopt the standard rate-and-state friction law, with the aging formulation for the state evolution (Dieterich, 1979, 1981; Ruina, 1983), and the shear stress τ that obeys the following equation:

$$\tau = \bar{\sigma} f = (\sigma - p)\left(f^* + a \ln \frac{V}{V^*} + b \ln \frac{V^* \theta}{L}\right) \quad , \tag{4}$$

where $\bar{\sigma}$ is the effective normal stress (the difference between the normal stress σ and the pore pressure p); f^* is the reference coefficient of friction at the reference slip rate V^*; and a, b, and L are rate-and-state parameters. Fault regions with $(a - b) > 0$ have steady state VS properties, which allow steady slip under loading, while fault regions with $(a - b) < 0$ have VW properties, which promote earthquake nucleation and stick-slip behavior over a large enough area.

For VW fault areas, the critical nucleation size, h^*, can be estimated as follows for a 2-D strike-slip fault and $0.5 < a/b < 1$ (Ampuero & Rubin, 2008):

$$h^* = \frac{2}{\pi} \frac{\mu b L}{(b - a)^2 \bar{\sigma}} \quad , \tag{5}$$

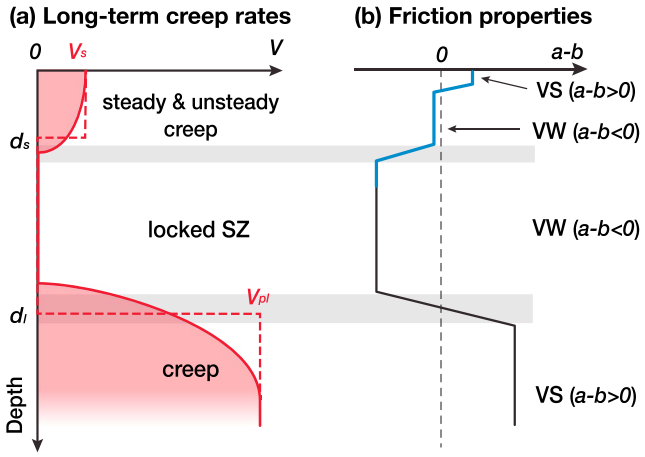

Figure 12. Simple models for fault slip and rheology of the southern San Andreas fault. (a) Creep on the fault occurs above and below the interseismically locked, seismogenic zone (SZ). The surface creep consists of steady creep and unsteady creep events, above the depth d_s; the average creep rate at the surface, V_s, is directly determined by d_s, the effective locking depth of the fault, d_l, and the long-term plate-loading rate, V_{pl}. The solid line indicates a stress-controlled crack model of deep creep that has similar stressing on the shallow fault, compared to the dislocation model (dashed line). (b) The shallow unsteady and steady fault creep can result from velocity-strengthening (VS; $a-b>0$) and mildly velocity-weakening (VW; $a-b<0$ and $a-b\sim 0$) frictional properties on top of the VW seismogenic zone and deeper VS fault extension. Horizontal bars in gray indicate locked-creeping transition zones. We impose fault slip rates in regions marked in black and solve for the fault stress, slip rate, and state variables in regions marked in blue.

where μ is the shear modulus. If h^* is larger than the size of the VW fault area, frictional instability can initiate in the form of transient accelerated creep but will not lead to seismic failure. We resort to this mechanism to produce spontaneous shallow slow slip in our models, similar to models for slow slip in subduction zones (e.g., Liu & Rice, 2007; Rubin, 2008). We adjust parameters a, b, and L to produce aseismic transients with periods of ~2 years, while altering the critical nucleation size to obtain maximum slip rates of up to $\sim 10^{-6}$ m/s in the models. Since the properties of the shallowest VS layer and mildly VW layer would trade off with each other in promoting/suppressing the amplitude of aseismic transients that propagate to the surface, we impose a thickness of 0.1–0.15 km for the VS layer and change other parameters to sustain prominent aseismic transients.

In addition, we choose the rate-and-state frictional parameters in our models to allow dynamic triggering of slip under stress perturbations of ~50 kPa. We notice that the millimeter-level-triggered slip in mildly VW regions occurs only when peak slip rates reach $\sim 10^{-3}$–10^{-5} m/s (from an initial slip rate of $\sim 10^{-10}$ m/s). Since the state variable θ does not yet change at the onset of triggered slip, from equation (4) we can derive $\Delta\tau = a\sigma \ln(V_f/V_i)$, in which the stress change $\Delta\tau$ is proportional to the change in logarithmic slip rates from an initial value V_i to a near-triggering value V_f . For a stress change of ~50 kPa, $a\sigma$ is estimated to be ~5 kPa. If σ is ~18 MPa at a depth of 1 km, the inferred value of a is $\sim 10^{-4}$, considerably lower than the laboratory-derived values of $\sim 10^{-3}$-10^{-2}. Assuming the laboratory-derived values of a would imply elevated (above-hydrostatic) pore fluid pressures.

Considering targeted model features and numerical stability, we adopt parameters a and b with values of ~0.002 or larger ($a = 0.0018$ and $b = 0.0022$ for mildly VW areas), a characteristic evolution distance L of 180 μm, and a depth-dependent effective normal stress following one third of the hydrostatic stress gradient, $\bar{\sigma} = 0.96+6z$ (MPa), where the depth z is in kilometers, a possible scenario due to fluid overpressure. Toward the surface, the effective normal stress is smaller, while the nucleation size is larger. We impose a minimum effective normal stress near the surface to avoid excessively large slip rate variations during the triggering process and associated numerical stability issues. The key model parameters and their values are listed in Table S1, and layered structure of fault frictional properties is listed in Table S2.

The combination of these fault parameters results in depth-dependent nucleation zone sizes and stability conditions in the shallow fault zones (Figure 13a). The mildly VW areas are conditionally stable and can

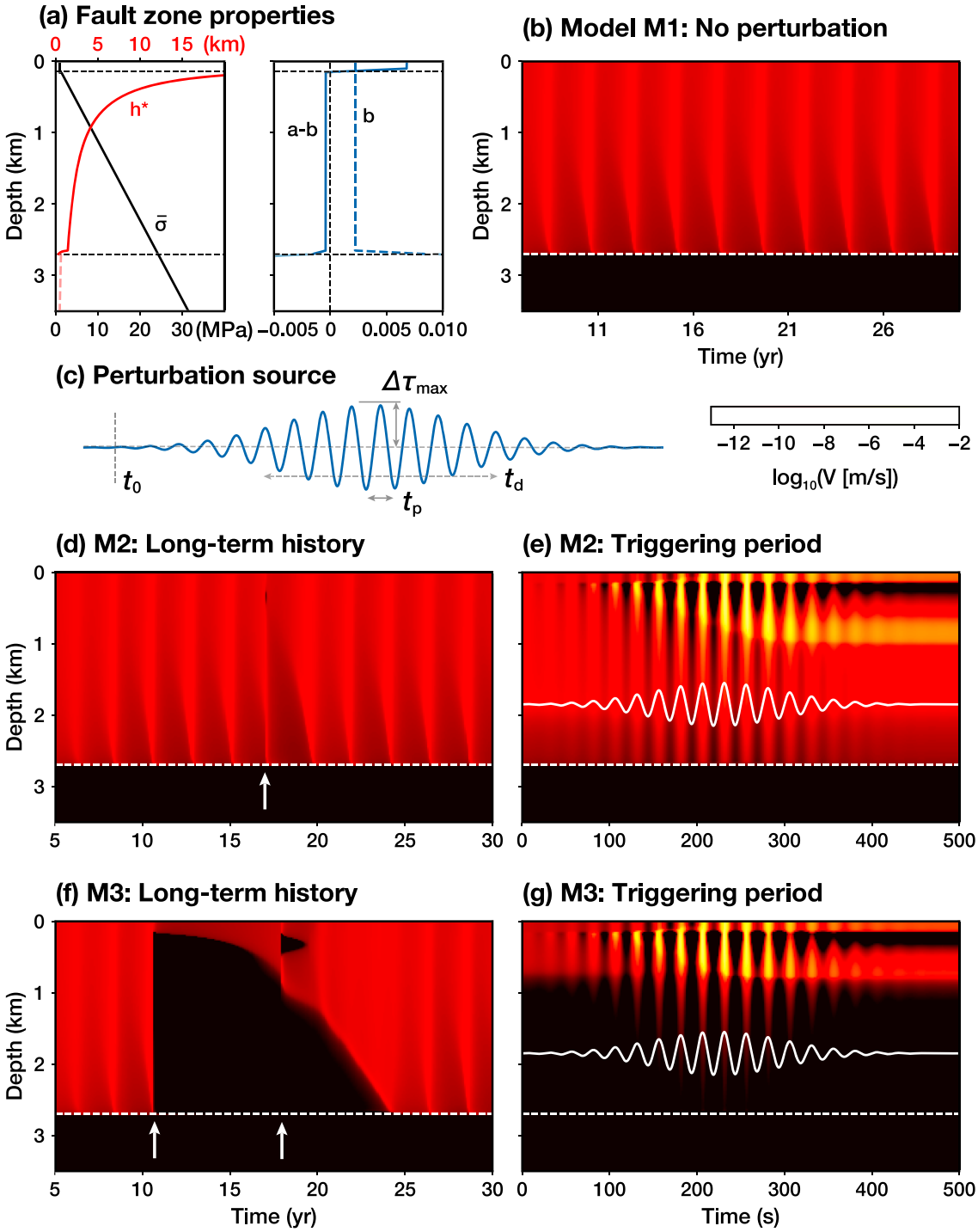

Figure 13. Depth-dependent fault properties and responses to dynamic perturbations. (a) Depth profiles of (left) the effective normal stress, $\bar{\sigma}$, and locally estimated nucleation size of velocity-weakening fault areas, h^* (solid red line; dashed line indicates the deeper seismogenic zone), and (right) rate-and-state frictional parameters (*a*-*b*; solid blue line) and *b* (dashed blue line). (b) The time evolution of logarithmic slip rates on the fault for the case without perturbations. (c) The temporal function of the applied dynamic stress perturbation, parameterized by the onset time, t_0, maximum dynamic Coulomb stress change, $\Delta\tau_{max}$, characteristic period, t_p, and duration, t_d. The responses of these shallow fault areas to dynamic perturbations are depth and history dependent. The time evolution of slip rates in these perturbed cases are shown for (d and e) a single dynamic perturbation ($\Delta\tau_{max}$ = 69 kPa) and (f and g) two consecutive dynamic perturbations ($\Delta\tau_{max}$ = 85 and 74 kPa, respectively). The left column (d and f) shows long-term slip history; the right column (e and g) shows the triggering period. White arrows mark the time of applied dynamic stress perturbations. The waveforms (white) in (g) are drawn to illustrate stress changes at corresponding time.

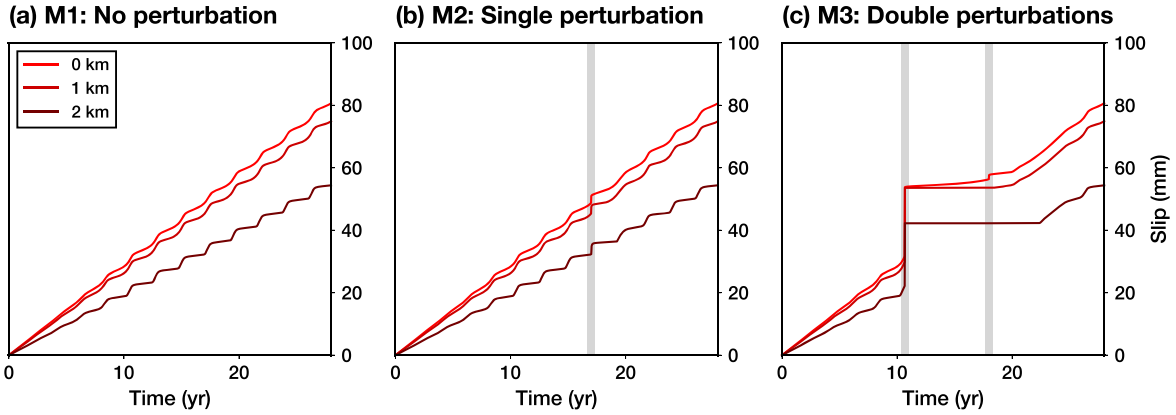

Figure 14. Time-dependent creep at different depths on the fault (0, 1, and 2 km) for Models M1–M3 (panels a-c, respectively). The vertical bars in gray indicate the timing of applied dynamic stress perturbations.

accommodate fault creep, together with the shallow VS layer, occasionally producing spontaneous aseismic transient creep (Figures 13b). These transient episodes arise as a result of shallow creep eroding into a nominally locked region at greater depths and initiating aseismic instability that can propagate updip across the entire shallow layer (Figure 13b). The larger variations in slip rates toward greater depths reflect the increased instability conditions due to increasing normal stress (Figure 14a).

To explore the fault creep triggering process in this model, we apply dynamic stress perturbations to the fault model using a simplified time-dependent function with the following parameterization (Figure 13c), motivated by seismic observations in section 3.2:

$$\Delta\tau(t) = \Delta\tau_{\max} \exp\left(-\frac{1}{2}\frac{(t - t_o - 1.5t_d)^2}{(t_d/2)^2}\right) \sin(2\pi t/T), \tag{6}$$

where $\Delta\tau_{\max}$ is the maximum amplitude of stress perturbation, t_o is the origin time of the perturbation, t_d is the half-duration of the perturbation source, and T is the characteristic period. We apply this stressing function uniformly along depth and only to the shear stress component. Since the coefficient of friction does not deviate from f^* significantly in time (Figures S12–S14), this simplification should yield qualitatively similar results compared to perturbations to both normal/shear stress components with the same Coulomb stress changes (Perfettini et al., 2003). The simplified form of stress perturbation allows us to focus on the first-order fault response and relation between physical variables during the triggering period.

We consider a suite of models (Figure 13) to illustrate the effect of dynamic stress perturbations on shallow fault creep. In Model M2 (Figures 13d and 13e), we apply a single dynamic perturbation after the model reaches near-periodic behavior, similar to M1 (Figure 13b; $\Delta\tau_{\max} = 69$ kPa; $t_o = 17$ year; $t_d = 150$ s; $T = 25$ s). The stress perturbation has the largest effect on slip rates in shallower fault zones due to the low effective normal stress (Figure 13e). During positive stress changes, once reaching a threshold value, the locally elevated slip rates in VW areas would lead to expanding (aseismic) failure of a larger fault area, propagating toward greater depths as well as the surface. Such an episode results in triggered slip of ~5 mm over the shallowest part of fault zone (Figure 14b).

In model M3, we apply two consecutive dynamic perturbations, with the first source ($\Delta\tau_{\max} = 85$ kPa; $t_o = 10.6$ year; $t_d = 60$ s; $T = 10$ s) preceding the second source by ~7.4 year ($\Delta\tau_{\max} = 74$ kPa; $t_o = 18$ year; $t_d = 150$ s; $T = 25$ s). Such a scenario could be applicable to fault areas that have experienced triggering due to prior larger perturbations, for example, the seismic waves from the 2010 El Mayor-Cucapah earthquake, and a later smaller perturbation. The first perturbation results in widespread slow slip of 20–30 mm in the entire shallow fault zone and locking of most fault areas in the following decade (Figures 13f, 13g, and 14c). The interseismic shallow creep recovers, starting from the surface, and erodes into the deeper locked zone. The second perturbation only triggers slip of ~2 mm, even with a stronger source than that in M2. The different behavior in M2 and M3 demonstrates that the triggering of fault creep depends not only on the properties of the perturbation source but also on fault creep history. More detailed behavior of models

M1–M3 are shown in Figures S12–S14. While our models demonstrate the possibility of reproducing triggered slip of ~1–10 mm under dynamic stress changes of ~50 kPa, the range of stress perturbations we have considered is relatively narrow and nonetheless produces a large variability in the amplitude of triggered slip. We further discuss the insights and limitations of our modeling and implications for shallow fault zone rheology in section 4.

4. Discussion

The InSAR, creepmeter, and field observations presented in section 2 document an accelerated shallow slip event that occurred along the ~40-km-long segment of the SSAF between Bombay Beach and Box Canyon. The creepmeter data that have the highest temporal resolution indicate that the onset of the slip event occurred within minutes of the passage of seismic waves from the 2017 M_w8.2 Chiapas earthquake (Figure 3), suggestive of dynamic triggering.

The decomposition of InSAR LOS measurements into horizontal and vertical components of motion, as shown in Figures 6, 8, and S8, provides an opportunity to examine the individual components of surface displacement that may be attributed to distinct deformation mechanisms. The fault-parallel displacements shown in Figures 9 and S10 dominate the deformation transient triggered by the 2017 Chiapas earthquake.

The inferred vertical displacements (Figure 6e) may result from a variety of processes, including natural and anthropogenic hydrologic effects, such as pumping and recharge cycles in the Coachella valley, and seasonal hydrologic fluctuations near the Salt Creek. There is evidence for a differential vertical motion across the fault trace, previously noted by Lindsey, Fialko, et al. (2014). However, the pattern seen in Figure 6e is opposite to that observed in previous years using ERS-1/2 (Fialko, 2006; Lyons & Sandwell, 2003; Manzo et al., 2012) and Envisat (Lindsey, Fialko, et al. 2014) data: We observe a relative uplift, rather than subsidence, on the western side of the fault along the Coachella valley segment. This reversal in the sense of vertical motion across the fault could be due to temporal variations in the pumping and recharge of water in the Coachella valley, influenced in part by multiyear regional variations in precipitation. Similar anomalous vertical deformation due to hydrological processes, specifically in the Coachella valley as well as other regions, has been observed in the past (Bawden et al., 2001; Schmidt et al., 2016; Wisely & Schmidt, 2010). Similar differential vertical motion can be observed along the fault trace farther to the south. Results shown in Figure 6 highlight the importance of using data from different lines of sight in studies of shallow fault creep.

We showed that filtering of radar interferograms introduces errors that scale up with the number of interferograms used in the analysis. This implies that the signal-to-noise ratio may not improve with adding more data, as commonly expected. A number of recent studies have attributed the phase nonclosure to physical processes, such as variations in soil moisture (e.g., Conde et al., 2018; Zan et al., 2014; Zwieback et al., 2016, 2017). However, our results indicate that phase inconsistencies emerge due to data processing, specifically filtering and/or multilooking of the radar phase, and do not affect the raw radar phase. This suggests that the phase nonclosure problem can be efficiently mitigated using the unfiltered phase. We proposed a simple algorithm for removing artifacts introduced by filtering of the radar phase.

The time series of surface deformation along the SSAF derived from Sentinel-1 data show the onset of accelerated creep around the time of the 2017 Chiapas earthquake (Figure 8). Because the algorithm used for atmospheric corrections works best for the gradually varying deformation signals, there is a certain amount of smearing of steps and rapid changes in surface velocities with time (e.g., Wang & Fialko, 2018). This may be responsible for the less impulsive onset of slip transient in the InSAR time series compared, for example, to the creepmeter observations, which have a much higher temporal resolution (Figure 3a); however, we cannot rule out a possibility that at some locations along the fault, a slow slip event was already underway at the time of the Chiapas earthquake.

In places that exhibit a good agreement between the magnitudes of surface slip measured by InSAR (sampling surface displacements at distances of a few hundred meters away from the fault trace) and creepmeter and geologic observations (Figure 9), most of slip is inferred to have occurred on a highly localized interface, possibly as narrow as a few millimeters (Figure 5), similar to earlier observations from the Superstition Hills Fault (Wei et al., 2009). At other locations where displacements recorded by creepmeters and geological

measurements are lower than those observed with InSAR, even if one takes into account uncertainties of each measurement (Figure 9), only a fraction of the total shear motion involved in the triggered slip event occurs within a few meters from the fault trace, and the remainder must be distributed in a broader shear zone. The effective width of the surface shear zone has practical implications for potential damage caused by creep on fault-crossing infrastructure such as canals, buried cables, and pipelines. The width of the shear zone also has implications for paleoseismic studies of fault slip, such that piercing point estimates of coseismic offsets may underestimate slip if the latter is distributed in a broader zone.

We have estimated an upper bound on the effective width of the surface shear zone involved in the slow slip event triggered by the Chiapas earthquake using three-piece linear fits to profiles of horizontal displacements (e.g., Lindsey, Fialko, et al., 2014). Results are shown in Figures S15 and S16. As one can see in Figure S16, the estimated width of the shear zone exceeds 100 m in several locations—in particular, near North Shore and at the southernmost end of the fault near Bombay Beach. The observed variations in the degree of slip localization along the SSAF may be related to the rheology of the uppermost ~100–200 m of the poorly consolidated sedimentary cover, as well as the stress conditions (Lindsey, Fialko, et al., 2014).

The data indicate that the magnitude of surface slip that occurred over ~6 months after the onset of the slow slip event varies along the strike of the SSAF, with highest magnitudes on the order of 15 mm (Figure 9). Interestingly, inversions of surface displacements indicate that the magnitude of surface slip appears to anticorrelate with the depth extent of slip. For example, at North Shore the best fitting values for the slip magnitude s_s and the depth extent of shallow slip d_s are 7 ± 0.5 mm and 1.4 ± 0.2 km, respectively (Site T4, Figure 10b). Smaller amplitudes (<6 mm) and greater depths (2–3 km) of shallow creep are inferred farther to the south (Figures 10c and 10d). This may be due to the spatiotempral variability in slip history in the shallow conditionally stable layer. The slip depths suggested by our inversions are comparable to the range of thicknesses of the sedimentary layer and the depth extent of creep reported by Sieh and Williams (1990). The inversions also suggest systematic increases in the fault dip angle from the Coachella Valley toward the Bombay Beach, consistent with models of Tymofyeyeva and Fialko (2018). At Box Canyon, inversions suggest a dip angle as small as ~50° and depth of slip of 0.5 km (Figure 10a). The abnormally shallow dip and depth of slip may be an artifact due to proximity to the northern terminus of triggered slip (Site T5, Figure 7b), that is, a 3-D effect that is not captured by the 2-D antiplane strain models. The attitude of the SSAF in the uppermost crust has been the subject of some debate. Fialko (2006) and Lindsey and Fialko (2013) suggested an average dip angle of 60–70° based on best fitting models of interseismic deformation and the fact that the same dip angle projects seismicity lineations to the surface trace of the SSAF (e.g., Lin et al., 2007). Fuis et al. (2017) suggested that the SSAF steepens toward the surface, based on the seismic reflectivity patterns around the fault trace in the top several kilometers of the Earth crust. Assuming that the slip interface that produces shallow creep connects to the seismogenic part of the SSAF, results shown in Figure 10 favor an eastward dipping geometry of the SSAF throughout all of the upper crust.

The average magnitude of surface slip triggered on the SSAF by the Chiapas earthquake is 5–10 mm (Figures 7b, 9, and 10). This is comparable to the magnitude of surface slip triggered by the 2010 El Mayor-Cucapah earthquake (e.g., Rymer et al., 2010; Wei et al., 2010), despite the fact that the stress changes presumably responsible for triggering the observed slip are different by several orders of magnitude. Lower surface creep rates on the SSAF observed prior to the Chiapas earthquake (Figures 8a and 7a) compared to the long-term average (e.g., Lindsey, Fialko, et al. 2014; Sieh & Williams, 1990) may result from an "overshoot" or a "stress shadow" from a robust shallow creep triggered by the 2010 El Mayor-Cucapah earthquake. A comparison of new data presented in this study with previously published results suggests that the rates of shallow creep on the SSAF may be approximately constant on time scales on the order of 10 years or greater but can vary considerably on shorter time scales.

The distribution of surface slip that occurred following the 2017 Chiapas earthquake (Figure 9) does not follow that observed between 2004 and 2010 (Lindsey, Fialko, et al., 2014, their figure 6a). Also, Lindsey, Fialko, et al. (2014) noted variations in the degree of localization of shallow creep such that the creep appears to be more localized in transpressional areas and more distributed in transtensional areas. The slow slip event triggered by the Chiapas earthquake does not follow the same pattern. In particular, we observe a fairly localized surface slip along the transtensional North Shore segment (Figure 9). This is also supported by the creepmeter data that showed a sizeable triggered slip event (Figure 3a) for the first time since the recording began in 2010.

The comparison of surface displacements that occurred over different epochs (e.g., Figure 9; Lindsey, Fialko, et al., 2014) suggests a complex spatiotemporal evolution of slip in the shallow conditionally stable layer, with triggered and spontaneous slip events occurring at variable depths and locations along strike. This is similar to the shallow slip histories reported at other locations (e.g., Bilham et al., 2016; Jolivet et al., 2015; Linde et al., 1996; Murray & Segall, 2005; Shirzaei & Bürgmann, 2013; Simpson et al., 2001; Wei et al., 2009). Alternatively, the observed variations in the effective width of the shear zone may be indicative of time-dependent strain localization within the shallow crust during the interseismic period.

The variability in the amplitude and depth extent of triggered creep on the SSAF may have several explanations. First, the frictional properties of the uppermost crust may be variable both downdip and along the strike, possibly with some stochastic distribution, similar to a model proposed by Jiang and Fialko (2016) for a transitional zone at the bottom of the seismogenic layer. Second, the dynamic perturbations on different parts of the shallow fault may be more variable than suggested by surface seismic observations. That, combined with the high sensitivity of such faults to stress perturbations, may lead to variability in triggered creep along the fault. Third, the behavior of triggered creep also depends on the past fault creep history at a given location. The timing of stress perturbations and the characteristic times of fault recovery to the unperturbed state may strongly influence the triggering thresholds, the magnitude of triggered slip, and the subsequent slip evolution.

Our models of rate-and-state faults share similar features near the surface with previously proposed models for shallow episodic fault creep (Wei et al., 2013; Wei, Yajing, et al., 2015); the differences in these models lie in how the conditionally stable region transitions to the seismogenic zone. The two types of models can both produce the spontaneous and triggered creep near the surface. A wider transitional zone with depth-dependent properties in our models may explain the variable depth extent of triggered creep in a single model setup suggesting that complexity in the triggered slip can be attributed to inherent fault creep dynamics. Nonetheless, the observed spatiotemporal complexity in triggered fault creep on SSAF suggests that 3-D models may be necessary to explain the data. The extremely low triggering stress, on the order of 10 kPa, implies extraordinary sensitivity of the shallow fault zone and yet much larger stress perturbations, for example, during the 2010 El Mayor-Cucapah earthquake ($\Delta\tau_{max}$ ~1 MPa; Wei, Yajing, et al., 2015) have not triggered a much larger slip compared to the 2017 event. Other physical processes, such as fault zone dilatancy (Segall & Rice, 1995), may contribute to the observed time dependence of shallow creep, or even be required to reconcile all observations. Combining more advanced models with the increasingly rich observational data sets will help further illuminate physical mechanisms of shallow creep and rheological properties of the uppermost crust for major faults such as the SSAF.

5. Conclusions

We presented geodetic and geologic measurements of a transient creep event on the SSAF that ruptured the shallow part of the fault from Bombay Beach to the Mecca Hills. The timing of the event suggests that it was triggered by dynamic stress changes from the 2017 M_w8.2 earthquake in Chiapas, Mexico. The creep event lasted several months and produced surface offsets of 4–12 mm, with considerable variations along the fault. Right-lateral creep was accompanied by differential vertical motion (east side down) across the fault trace, reversing the long-term trend observed since the last century. InSAR data suggest that the width of the surface shear zone associated with surface creep is greater than 100 m at some locations along strike. At these locations (e.g., Ferrum and North Shore), observations from creepmeters that have spatial aperture of several meters record 40–60% of surface shear documented by InSAR measurements, implying that the remainder is distributed across a broader shear zone. At other sites along the fault, a good agreement between the low-aperture creepmeter and geological measurements, and the InSAR data sampled at 100-m resolution, indicates that most of the deformation is localized on a fault interface, in some places possibly as narrow as a few millimeters. The slow slip event triggered by the 2017 Chiapas earthquake is comparable in magnitude to the triggered slip due to the 2010 El Mayor-Cucapah earthquake. A comparison of the new data with previously published results suggests that the rates of shallow creep on the SSAF may be essentially constant on time scales on the order of 10 years or greater but can vary considerably on shorter time scales. A 2-D fault zone model assuming monotonic variations in the velocity-dependence parameter ($a-b$) is able to reproduce a number of features in the observed slip histories. However, more complicated models, including stochastic variations in the rate-and-state parameters and rate-dependent hardening mechanisms such as dilatancy,

may be required to fit all of the available data. Such models may ultimately help refine our knowledge of potential connections between shallow creep events and earthquakes.

Acknowledgments
We thank two anonymous reviewers for insightful and detailed reviews. This study was supported by NASA (Grant 80NSSC18K0466) and NSF (Grant EAR-1841273). Sentinel-1 data were provided by the European Space Agency (ESA) through Alaska Satellite Facility (ASF) and UNAVCO. Digital Elevation data were provided by DLR. Some of the figures were generated using the Generic Mapping Tools (GMT; Wessel et al., 2013). The numerical simulations used the Extreme Science and Engineering Discovery Environment (XSEDE) COMET cluster at the San Diego Supercomputer Center (SDSC) through Allocation EAR-170014. The data that support the research and visualizations in this paper are available online (at http://igppweb.ucsd.edu/~fialko/Assets/Data/ssaf_creep.tar.gz).

References

Allen, C. R., Wyss, M., Brune, J. N., Grantz, A., & Wallace, R. E. (1972). Displacements on the Imperial, Superstition Hills, and San Andreas Faults triggered by the Borrego Mountain earthquake (*787*). Washington, DC: Geological Survey Professional Paper. pp. 87–104.

Ampuero, J.-P., & Rubin, A. M. (2008). Earthquake nucleation on rate and state faults—Aging and slip laws. *Journal of Geophysical Research*, *113*, B01302. https://doi.org/10.1029/2007JB005082

Araki, E., Saffer, D. M., Kopf, A. J., Wallace, L. M., Kimura, T., Machida, Y., et al. IODP Expedition 365 shipboard scientists (2017). Recurring and triggered slow-slip events near the trench at the Nankai Trough subduction megathrust. *Science*, *356*(6343), 1157–1160.

Bawden, G. W., Thatcher, W., Stein, R. S., Hudnut, K. W., & Peltzer, G. (2001). Tectonic contraction across Los Angeles after removal of groundwater pumping effects. *Nature*, *412*(6849), 812.

Behr, W., Rood, D., Fletcher, K., Guzman, N., Finkel, R., Hanks, T. C., et al. (2010). Uncertainties in slip-rate estimates for the Mission Creek strand of the southern San Andreas fault at Biskra Palms Oasis, southern California. *GSA Bulletin*, *122*(9-10), 1360–1377.

Bilham, R., & Behr, J. (1992). A two-layer model for aseismic slip on the Superstition Hills fault, California. *Bulletin of the Seismological Society of America*, *82*(3), 1223–1235.

Bilham, R., Ozener, H., Mencin, D., Dogru, A., Ergintav, S., Cakir, Z., et al. (2016). Surface creep on the North Anatolian fault at Ismetpasa, Turkey, 1944–2016. *Journal of Geophysical Research: Solid Earth*, *121*, 7409–7431. https://doi.org/10.1002/2016JB013394

Bilham, R., Suszek, N., & Pinkney, S. (2004). California creepmeters. *Seismological Research Letters*, *75*(4), 481–492.

Bilham, R., & Williams, P. (1985). Sawtooth segmentation and deformation processes on the southern San Andreas fault, California. *Geophysical Research Letters*, *12*(9), 557–560.

Cakir, Z., Akoglu, A. M., Belabbes, S., Ergintav, S., & Meghraoui, M. (2005). Creeping along the Ismetpasa section of the North Anatolian fault (Western Turkey): Rate and extent from InSAR. *Earth and Planetary Science Letters*, *238*, 225–234.

Chen, C. W., & Zebker, H. A. (2000). Network approaches to two-dimensional phase unwrapping: Intractability and two new algorithms. *Journal of the Optical Society of America A*, *17*(3), 401–414. https://doi.org/10.1364/JOSAA.17.000401

Conde, V., Catalão, J., Nico, G., & Benevides, P. (2018). High resolution mapping of soil moisture in agriculture based on Sentinel-1 interferometric data, *Remote Sensing for Agriculture, Ecosystems, and Hydrology XX* (Vol. 10783, pp. 107831U). Portugal: International Society for Optics and Photonics. https://doi.org/10.1117/12.2325709

Dieterich, J. H. (1979). Modeling of rock friction. 1. Experimental results and constitutive equations. *Journal of Geophysical Research*, *84*(NB5), 2161–2168. https://doi.org/10.1029/JB084iB05p02161

Dieterich, J. H. (1981). Potential for geophysical experiments in large scale tests. *Geophysical Research Letters*, *8*(7), 653–656. https://doi.org/10.1029/GL008i007p00653/pdf

Fialko, Y. (2006). Interseismic strain accumulation and the earthquake potential on the southern San Andreas fault system. *Nature*, *441*, 968–971.

Fialko, Y., Sandwell, D., Agnew, D., Simons, M., Shearer, P., & Minster, B. (2002). Deformation on nearby faults induced by the 1999 Hector Mine earthquake. *Science*, *297*(5588), 1858–1862. https://doi.org/10.1126/science.1074671

Fialko, Y., Simons, M., & Agnew, D. (2001). The complete (3-D) surface displacement field in the epicentral area of the 1999 MW7.1 Hector Mine Earthquake, California, from space geodetic observations. *Geophysical Research Letters*, *28*(16), 3063–3066. https://doi.org/10.1029/2001GL013174

Fuis, G. S., Bauer, K., Goldman, M. R., Ryberg, T., Langenheim, V. E., Scheirer, D. S., et al. (2017). Subsurface geometry of the San Andreas fault in southern California: Results from the Salton Seismic Imaging Project (SSIP) and strong ground motion expectations. *Bulletin of the Seismological Society of America*, *107*(4), 1642–1662.

Goldstein, R. M., & Werner, C. L. (1998). Radar interferogram filtering for geophysical applications. *Geophysical Research Letters*, *25*(21), 4035–4038. https://doi.org/10.1029/1998GL900033

Gomberg, J., & Bodin, P. (1994). Triggering of the Ms = 5.4 Little Skull Mountain, Nevada, earthquake with dynamic strains. *Bulletin of the Seismological Society of America*, *84*(3), 844–853.

Goulty, N. R., & Gilman, R. (1978). Repeated creep events on the San Andreas fault near Parkfield, California, recorded by a strainmeter array. *Journal of Geophysical Research*, *83*(B11), 5415–5419. https://doi.org/10.1029/JB083iB11p05415

Harris, R. A. (2017). Large earthquakes and creeping faults. *Reviews of Geophysics*, *55*, 169–198. https://doi.org/10.1002/2016RG000539

Hauksson, E., Yang, W., & Shearer, P. M. (2012). Waveform relocated earthquake catalog for southern California (1981 to June 2011). *Bulletin of the Seismological Society of America*, *102*(5), 2239–2244.

Heidarzadeh, M., Ishibe, T., & Harada, T. (2018). Constraining the source of the Mw 8.1 Chiapas, Mexico earthquake of 8 September 2017 using teleseismic and tsunami observations. *Pure and Applied Geophysics*, *175*(6), 1925–1938. https://doi.org/10.1007/s00024-018-1837-6

Jänecke, S. U., Markowski, D. K., Evans, J. P., Persaud, P., & Kenney, M. (2018). Durmid ladder structure and its implications for the nucleation sites of the next M > 7.5 earthquake on the San Andreas fault or Brawley seismic zone in southern California. *Lithosphere*, *10*, 1–30. https://doi.org/10.1130/L629.1

Jennings, C., & Bryant, W. (2010). *Fault activity map of California*, California Division of Mines and Geology, Geologic Data Map No. 6. California: California Geological Survey.

Jiang, J., & Fialko, Y. (2016). Reconciling seismicity and geodetic locking depths on the Anza section of the San Jacinto fault. *Geophysical Research Letters*, *43*, 10,663–10,671. https://doi.org/10.1002/2016GL071113

Jimenez, C. (2018). Seismic source characteristics of the intraslab 2017 Chiapas-Mexico earthquake (Mw8.2). *Physics of the Earth and Planetary Interiors*, *280*, 69–75. https://doi.org/10.1016/j.pepi.2018.04.013

Jolivet, R., Simons, M., Agram, P., Duputel, Z., & Shen, Z.-K. (2015). Aseismic slip and seismogenic coupling along the central San Andreas Fault. *Geophysical Research Letters*, *42*, 297–306. https://doi.org/10.1002/2014GL062222

Kaneko, Y., Fialko, Y., Sandwell, D. T., Tong, X., & Furuya, M. (2013). Interseismic deformation and creep along the central section of the North Anatolian Fault (Turkey): InSAR observations and implications for rate-and-state friction properties. *Journal of Geophysical Research: Solid Earth*, *118*, 316–331. https://doi.org/10.1029/2012JB009661

LaBonte, A., Brown, K., & Fialko, Y. (2009). Hydrogeologic detection and finite-element modeling of a slow-slip event in the Costa Rica prism toe. *Journal of Geophysical Research*, *114*, B00A02. https://doi.org/10.1029/2008JB005806

Lau, N., Tymofyeyeva, E., & Fialko, Y. (2018). Variations in the long-term uplift rate due to the Altiplano-Puna magma body observed with Sentinel-1 interferometry. *Earth and Planetary Science Letters*, *491*, 43–47.

Li, V. C., & Rice, J. (1987). Crustal deformation in great California earthquake cycles. *Journal of Geophysical Research*, *92*, 11,533–11,551.
Lin, G., Shearer, P. M., & Hauksson, E. (2007). Applying a three-dimensional velocity model, waveform cross correlation, and cluster analysis to locate southern California seismicity from 1981 to 2005. *Journal of Geophysical Research*, *112*, B12309. https://doi.org/10.1029/2007JB004986
Linde, A. T., Gladwin, M. T., Johnston, M. J., Gwyther, R. L., & Bilham, R. G. (1996). A slow earthquake sequence on the San Andreas fault. *Nature*, *383*(6595), 65.
Lindsey, E., & Fialko, Y. (2013). Geodetic slip rates in the Southern San Andreas Fault System: Effects of elastic heterogeneity and fault geometry. *Journal of Geophysical Research: Solid Earth*, *118*, 689–697. https://doi.org/10.1029/2012JB009358
Lindsey, E. O., & Fialko, Y. (2016). Geodetic constraints on frictional properties and earthquake hazard in the Imperial Valley, Southern California. *Journal of Geophysical Research: Solid Earth*, *121*, 1097–1113. https://doi.org/10.1002/2015JB012516
Lindsey, E. O., Fialko, Y., Bock, Y., Sandwell, D. T., & Bilham, R. (2014). Localized and distributed creep along the southern San Andreas Fault. *Journal of Geophysical Research: Solid Earth*, *119*, 7909–7922. https://doi.org/10.1002/2014JB011275
Lindsey, E. O., Sahakian, V. J., Fialko, Y., Bock, Y., Barbot, S., & Rockwell, T. K. (2014). Interseismic strain localization in the San Jacinto fault zone. *Pure and Applied Geophysics*, *171*(11), 2937–2954. https://doi.org/10.1007/s00024-013-0753-z
Liu, Y., & Rice, J. R. (2007). Spontaneous and triggered aseismic deformation transients in a subduction fault model. *Journal of Geophysical Research*, *112*, B09404. https://doi.org/10.1029/2007JB004930
Louie, J., Allen, C., Johnson, D., Haase, P., & Cohn, S. (1985). Fault slip in southern California. *Bulletin of the Seismological Society of America*, *75*, 811–833.
Lyons, S., & Sandwell, D. (2003). Fault creep along the southern San Andreas from interferometric synthetic aperture radar, permanent scatterers, and stacking. *Journal of Geophysical Research*, *108*(B1), 2047. https://doi.org/10:1029/2002JB001831
Manzo, M., Fialko, Y., Casu, F., Pepe, A., & Lanari, R. (2012). A quantitative assessment of DInSAR measurements of interseismic deformation: The Southern San Andreas Fault case study. *Pure and Applied Geophysics*, *168*, 195–210.
Marone, C., & Scholz, C. H. (1988). The depth of seismic faulting and the upper transition from stable to unstable slip regimes. *Geophysical Research Letters*, *15*, 621–624.
McGill, S. F., Allen, C. R., Hudnut, K. W., Johnson, D. C., Miller, W. F., & Sieh, K. E. (1989). Slip on the Superstition Hills fault and on nearby faults associated with the 24 November 1987 Elmore Ranch and Superstition Hills earthquakes, southern California. *Bulletin of the Seismological Society of America*, *79*(2), 362–375.
Moreira, A., Krieger, G., Hajnsek, I., Hounam, D., Werner, M., Riegger, S., & Settelmeyer, E. (2004). TanDEM-X: A TerraSAR-X add-on satellite for single-pass SAR interferometry, *IGARSS 2004. 2004 IEEE International Geoscience and Remote Sensing Symposium* (Vol. 2, pp. 1000–1003). Anchorage, AK, USA: IEEE.
Murray, J., & Segall, P. (2005). Spatiotemporal evolution of a transient slip event on the San Andreas fault near Parkfield, California. *Journal of Geophysical Research*, *110*, B09407. https://doi.org/10.1029/2005JB003651
Neal, R. M. (2003). Slice sampling. *The Annals of Statistics*, *31*(3), 705–767. https://doi.org/10.1214/aos/1056562461
Obara, K., Hirose, H., Yamamizu, F., & Kasahara, K. (2004). Episodic slow slip events accompanied by non-volcanic tremors in southwest Japan subduction zone. *Geophysical Research Letters*, *31*, L23602. https://doi.org/10.1029/2004GL020848
Perfettini, H., Schmittbuhl, J., & Cochard, A. (2003). Shear and normal load perturbations on a two-dimensional continuous fault: 2. Dynamic triggering. *Journal of Geophysical Research*, *108*(B9), 863. https://doi.org/10.1029/2002JB001805
Rogers, G., & Dragert, H. (2003). Episodic tremor and slip on the Cascadia subduction zone: The chatter of silent slip. *Science*, *300*, 1942.
Rubin, A. M. (2008). Episodic slow slip events and rate-and-state friction. *Journal of Geophysical Research*, *113*, B01302. https://doi.org/10.1029/2008JB005642
Ruina, A. (1983). Slip instability and state variable friction laws. *Journal of Geophysical Research*, *88*(B12), 10,359–10,370. https://doi.org/10.1029/JB088iB12p10359
Rymer, M. (2000). Triggered surface slips in the Coachella Valley area associated with the 1992 Joshua Tree and Landers, California, earthquakes. *Bulletin of the Seismological Society of America*, *90*, 832–848.
Rymer, M. J., Boatwright, J., Seekins, L. C., Yule, J. D., & Liu, J. (2002). Triggered surface slips in the Salton Trough associated with the 1999 Hector Mine, California, earthquake. *Bulletin of the Seismological Society of America*, *92*(4), 1300–1317. https://doi.org/10.1785/0120000935
Rymer, M. J., Treiman, J. A., Kendrick, K. J., Lienkaemper, J. J., Weldon, R. J., Bilham, R., et al. (2010). Triggered surface slips in southern California associated with the 2010 El Mayor-Cucapah (Tech. Rep.) Baja California, Mexico, earthquake: U.S. Geological Survey Open-File Report 2010–1333.
Savage, J., & Lisowski, M. (1993). Inferred depth of creep on the Hayward fault, central California. *Journal of Geophysical Research*, *98*, 787–793.
Schmidt, D., Tong, X., Barbour, A., & Sandwell, D. (2016). Recovering vertical and time-dependent deformation near Coachella Valley (*SCEC Award 15108*). California: California with InSAR.
Schulz, S., Burford, R. O., & Mavko, B. (1983). Influence of seismicity and rainfall on episodic creep on the San Andreas Fault System in central California. *Journal of Geophysical Research*, *88*(B9), 7475–7484. https://doi.org/10.1029/JB088iB09p07475
Schwartz, S. Y., & Rokosky, J. M. (2007). Slow slip events and seismic tremor at circum-Pacific subduction zones. *Reviews of Geophysics*, *45*, RG3004. https://doi.org/10.1029/2006RG000208
Segall, P., & Rice, J. R. (1995). Dilatancy, compaction, and slip instability of a fluid-infiltrated fault. *Journal of Geophysical Research*, *100*(B11), 22,155–22,171.
Shifflett, H., Gray, M. G., Grannell, R., & Ingram, B. L. (2002). New evidence on the slip rate, renewal time, and Late Holocene surface displacement, southernmost San Andreas fault, Mecca Hills, California. *Bulletin of the Seismological Society of America*, *92*(7), 2861. https://doi.org/10.1785/0120000601
Shirzaei, M., & Bürgmann, R. (2013). Time-dependent model of creep on the hayward fault from joint inversion of 18 years of InSAR and surface creep data. *Journal of Geophysical Research: Solid Earth*, *118*, 1733–1746. https://doi.org/10.1002/jgrb.50149
Sieh, K., & Williams, P. (1990). Behavior of the southernmost San Andreas fault during the past 300 years. *Journal of Geophysical Research*, *95*, 6629–6645.
Simpson, R. W., Lienkaemper, J. J., & Galehouse, J. S. (2001). Variations in creep rate along the Hayward Fault, California, interpreted as changes in depth of creep. *Geophysical Research Letters*, *28*(11), 2269–2272. https://doi.org/10.1029/2001GL012979
Tong, X., Sandwell, D. T., & Smith-Konter, B. (2013). High-resolution interseismic velocity data along the San Andreas fault from GPS and InSAR. *Journal of Geophysical Research: Solid Earth*, *118*, 369–389. https://doi.org/10.1029/2012JB009442
Tymofyeyeva, E., & Fialko, Y. (2015). Mitigation of atmospheric phase delays in InSAR data, with application to the eastern California shear zone. *Journal of Geophysical Research: Solid Earth*, *120*, 5952–5963. https://doi.org/10.1002/2015JB011886

Tymofyeyeva, E., & Fialko, Y. (2018). Geodetic evidence for a blind fault segment at the southern end of the San Jacinto Fault Zone. *Journal of Geophysical Research: Solid Earth*, *123*, 878–891. https://doi.org/10.1002/2017JB014477

van der Woerd, J., Klinger, Y., Sieh, K., Tapponnier, P., Ryerson, F., & Meriaux, A. (2006). Long-term slip rate of the southern San Andreas Fault from ^{10}Be-^{26}Al surface exposure dating of an offs et alluvial fan. *Journal of Geophysical Research*, *111*, B04407. https://doi.org/10.1029/2004JB003559

Wallace, L. M., Webb, S. C., Ito, Y., Mochizuki, K., Hino, R., Henrys, S., et al. (2016). Slow slip near the trench at the Hikurangi subduction zone, New Zealand. *Science*, *352*(6286), 701–704.

Wang, K., & Fialko, Y. (2018). Observations and modeling of co- and postseismic deformation due to the 2015 M_w 7.8 Gorkha (Nepal) earthquake. *Journal of Geophysical Research: Solid Earth*, *123*, 761–779. https://doi.org/10.1002/2017JB014620

Wang, K., Xu, X., & Fialko, Y. (2017). Improving burst alignment in TOPS interferometry with bivariate enhanced spectral diversity (BESD). *IEEE Geoscience and Remote Sensing Letters*, *14*, 2423–2427.

Wei, M., Kaneko, Y., Liu, Y., & McGuire, J. J. (2013). Episodic fault creep events in California controlled by shallow frictional heterogeneity. *Nature Geoscience*, *6*, 566. https://doi.org/10.1038/ngeo1835

Wei, M., Liu, Y., Kaneko, Y., McGuire, J. J., & Bilham, R. (2015). Dynamic triggering of creep events in the Salton Trough, Southern California by regional. https://doi.org/10.1016/j.epsl.2015.06.044

Wei, M., Sandwell, D., & Fialko, Y. (2009). A silent M4.8 slip event of October 3–6, 2006, on the Superstition Hills fault, Southern California. *Journal of Geophysical Research*, *B07402*, 114. https://doi.org/10.1029/2008JB006135

Wei, M., Sandwell, D., Fialko, Y., & Bilham, R. (2010). Slip on faults in the Imperial Valley triggered by the 4 April 2010 Mw 7.2 El Mayor-Cucapah earthquake revealed by InSAR. *Geophysical Research Letters*, *38*, L01308. https://doi.org/10.1029/2010GL045235

Wei, M., Yajing, L., Yoshihiro, K., McGuire, J. J., & Bilham, R. (2015). Dynamic triggering of creep events in the Salton Trough, Southern California by regional M>5.4 earthquakes constrained by geodetic observations and numerical simulations. *Earth and Planetary Science Letters*, *427*, 1–10. https://doi.org/10.1016/j.epsl.2015.06.044

Wessel, P., Smith, W. H. F., Scharroo, R., Luis, J., & Wobbe, F. (2013). Generic mapping tools: Improved version released. *Eos, Transactions American Geophysical Union*, *94*(45), 409–410. https://doi.org/10.1002/2013EO450001

Wisely, B. A., & Schmidt, D. (2010). Deciphering vertical deformation and poroelastic parameters in a tectonically active fault-bound aquifer using InSAR and well level data, San Bernardino basin, California. *Geophysical Journal International*, *181*(3), 1185–1200. https://doi.org/10.1111/j.1365-246X.2010.04568.x

Xu, X., Sandwell, D., Tymofyeyeva, E., González-Ortega, A., & Tong, X. (2016). Tectonic and anthropogenic deformation at the Cerro Prieto geothermal step-over revealed by Sentinel-1A InSAR. *IEEE Transactions on Geoscience and Remote Sensing*, *55*, 5284–5292.

Zan, F. D., Parizzi, A., Prats-Iraola, P., & Lapez-Dekker, P. (2014). A sar interferometric model for soil moisture. *IEEE Transactions on Geoscience and Remote Sensing*, *52*(1), 418–425. https://doi.org/10.1109/TGRS.2013.2241069

Zwieback, S., Hensley, S., & Hajnsek, I. (2017). Soil moisture estimation using differential radar interferometry: Toward separating soil moisture and displacements. *IEEE Transactions on Geoscience and Remote Sensing*, *55*(9), 5069–5083. https://doi.org/10.1109/TGRS.2017.2702099

Zwieback, S., Liu, X., Antonova, S., Heim, B., Bartsch, A., Boike, J., & Hajnsek, I. (2016). A statistical test of phase closure to detect influences ondinsardeformation estimates besides displacements and decorrelation noise: Two case studies in high-latitude regions. *IEEE Transactions on Geoscience and Remote Sensing*, *54*(9), 5588–5601. https://doi.org/10.1109/TGRS.2016.2569435